Transport phenomena and correlation dynamics of a one-dimensional effective Hamiltonian equivalent to the hexagonal Harper model

Santanu Dhara, Dibyajyoti Sahu, Manvendra Singh, and Suhas Gangadharaiah

Department of Physics, Indian Institute of Science Education and Research, Bhopal 462066, India

The phase diagram of the one-dimensional hexagonal Harper (HH) model reveals the presence of two metallic phases and one insulating phase, separated by critical lines and a bicritical point. In our work, we investigate transport in the different phases by considering both the isolated and open system scenario. For the case of the isolated system, we study the single-particle dynamics at the bicritical point and along the critical lines. We find that the single-particle wave packet dynamics is superdiffusive in the critical regions with the transport at the bicritical point faster than that along the critical lines. In addition, we study domain wall (DW) dynamics via unconventional multiparticle states in the two metallic phases. The DW state is constructed by partially filling half of the chain while the other half is kept empty; the dynamics of this state reveals distinct behavior in the deep metallic regime of the two metallic phases. Interestingly, the distinct behavior is absent if one instead considers a fully filled half chain. For the open system scenario, we study transport in the nonequilibrium steady state (NESS). We observe that in the critical regions, transport is subdiffusive in nature. Moreover, we find that the transport scaling exponents for the open system scenario are the same at the bicritical point and along the critical lines, unlike the closed system case. In addition, we observe an even-odd size effect on the NESS density and current and on the optimal system-bath coupling parameter (corresponding to the maximum current) in the deep metallic regime of the HH model.

I. INTRODUCTION

Over the years a number of works have focused on understanding nonequilibrium quantum dynamics particularly in the context of transport, thermalization, and many-body localization in low-dimensional many-body quantum systems [1–6]. These studies have turned out to be crucial for understanding how a system relaxes toward a stationary state and the transport of conserved charges across it. In the case of integrable systems with an infinite number of local conserved quantities, the transport is ballistic in nature and the system acquires a stationary state described by the generalized Gibbs ensemble. However, in the presence of strong spatial disorder, transport is suppressed, which results in the localization phenomena [7–9]. Interestingly, a class of nonintegrable systems with correlated disorder, such as quasiperiodic models, has been found to exhibit anomalous transport [10–12].

Recent studies on quasiperiodic systems, in particular the Aubry-André-Harper (AAH) model, have attracted tremendous interest due to the system's anomalous transport properties and the localization transition [10,11,13–16]. One of the interesting feature of the AAH model is that at the critical point the eigenspectrum and eigenstates exhibit multifractality. The transport at the critical point is hampered since the single-particle eigenstates are not completely delocalized throughout the system. Recently, it was shown that the transport at the critical point of the AAH model exhibits contrasting behavior for the isolated and open system scenarios with the transport being superdiffusive and subdiffusive, respectively [12]. Moreover, it was found that the transport becomes diffusive with respect to any quasiperiodic disorder

in the presence of (local) dephasing [17]. While the transport behavior for the AAH model has been studied extensively, it is worth exploring whether these results hold for the other quasiperiodic systems.

The quasiperiodic one-dimensional (1D) AAH model is a particular case of the extended Harper model, where the latter is an effective 1D Hamiltonian describing the motion of a charged particle on a square (with next-nearest-neighbor hopping) or triangular lattice in the presence of a uniform magnetic field [18–20]. In the present work, we focus on an effective 1D Harper model which emerges from a two-dimensional (2D) tight-binding model on a honeycomb lattice with anisotropic hopping parameters in the presence of the magnetic field. We call this the hexagonal Harper (HH) model. Interestingly, unlike the 1D AAH model where the quasiperiodicity is present in the on-site term, in the HH model the quasiperiodicity is present in the hopping term while there is no on-site term. The phase diagram as a function of the anisotropy term differs from that of the extended Harper model. The phase diagram (see Fig. 1) exhibits two metallic regions and an insulating region, each of the phases separated by critical lines, and also a bicritical point where all three phases meet [21,22].

One of the primary reasons to study the HH model is that the dynamic aspects of this model have not received much attention in the literature thus far. The studies so far have found the spectrum for the anisotropic case [23], the characterization of the gap from the calculation of the bulk Chern number [21], and the characterization of the various phases via the fidelity, fidelity susceptibility, von Neumann entropy (VNE), and multifractal analysis [19,20,22,24,25]. Surprisingly, these
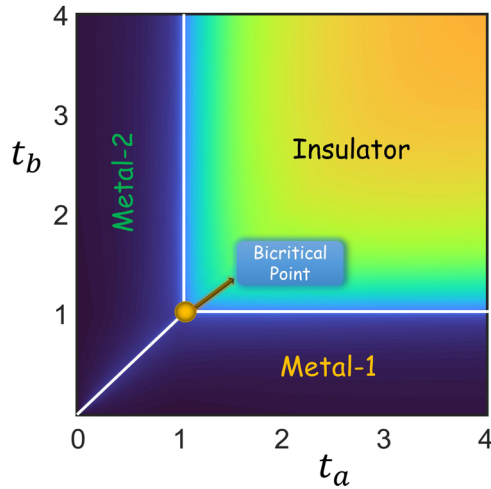
FIG. 1. The phase diagram of 1D HH model has been plotted by considering the analysis of average inverse participation ratio while setting the parameters $\phi = (\sqrt{5} - 1)/2$ and $k_x, k_y = 0$. The bicritical point is found at $t_a = 1 = t_b$, where the two metallic phases and one insulating phase meet. For $t_b \neq t_a$, $t_b < 1$ is the metallic regime 1 while $t_a < 1$ is the metallic regime 2. The three critical lines are as follows: metal-1-insulator line ($t_b = 1, t_a > 1$), metal-2-insulator line ($t_a = 1, t_b > 1$), and metal-1-metal-2 critical line ($t_a = t_b < 1$).

static quantifiers are incapable of distinguishing between the two metallic regimes. This motivates us to investigate whether the dynamical features of these two metallic regimes are identical. A second point of interest is to determine whether the transport scaling exponents differ at the different critical regimes of the 1D HH model for the closed and open system scenarios.

In the isolated system scenario, we find that the single-particle dynamics in the critical regions is superdiffusive. Interestingly, the scaling features for the two-point fermionic correlators differ at the bicritical point compared to the metal-insulator transition line and the metal-1-metal-2 transition line with the spread of the two-point correlators faster at the bicritical point. In the open scenario, we observe subdiffusive transport in the critical regions with the same scaling exponents along the entire critical regions. However, the transport scaling exponent for both the isolated and open transport differs between the HH and AAH models.

To further investigate the quantum many-body dynamics in the metallic phases we study the domain wall (DW) dynamics. Recently, a significant emphasis has been placed on the preparation of the inhomogeneous initial states for the study of the correlation spreading in quantum many-body systems [26–28]. The typical domain wall state is constructed by following the prescription of the ground state approach (GSA) as discussed in [29,30]. However, for the case of quasiperiodic systems, the GSA fails to produce the desired initial state (see Appendix B). Alternate approaches considering the exotic states such as the GSG (Ghosh-Singh-Gangadharaiah) state [26], rainbow state [31], and Dicke state [32] have been explored both theoretically and experimentally to construct the desired initial states. These choices have become feasible due to the advances in experimental controllability [32–36]. We prepare the DW with the GSG state and the entangled

state. We observe that in the deep metallic regime, the metallic phase 1 and phase 2 exhibit different transient behavior which has not been reported previously. Furthermore, we observe similarities in particle transport between one of the metallic phases in the HH model and the metallic phase of the AAH model.

We also find an that an intriguing odd-even size effect emerges in the NESS particle density and current within both the metallic phases under open system conditions. Specifically, the particle density acquires a constant (at 0.5) value for the even system sizes, while for odd system sizes, it can be manipulated by tuning the hopping parameters. Interestingly, we find that for the deep metallic regime, there is an optimal system-bath coupling parameter for which the nonequilibrium steady state (NESS) current is maximum. Moreover, the optimal system-bath coupling parameter can be determined by the anisotropic hopping parameters.

The outline of the paper is as follows. In Sec. II, we discuss the HH model Hamiltonian. This is followed by the study of single-particle dynamics in the different critical regions in Sec. III. In Sec. IV, we study the cross-correlation dynamics by considering the multiparticle GSG state and the multi-particle entangled state. We characterize the metallic phases by their transport properties in Sec. V. The open transport scenario has been considered in Sec. VI, in which we study the NESS particle density and the NESS current. Finally, we conclude our work in Sec. VII.

II. MODEL HAMILTONIAN AND THE PHASE DIAGRAM

In the context of quantum Hall effect physics, the study of electrons in a 2D periodic potential has received much attention [19,21,23,37,38]. Two such popular models include the 2D square lattice with next-nearest-neighbor hopping and the 2D triangular lattice with the nearest-neighbor hopping [19,23,38]. The 1D Hamiltonian derived from the above 2D Hamiltonian is called the generalized Harper model (GHM). Consider, for example, the GHM corresponding to the triangular lattice given by

$$H = -t\left[\sum_s \left(\left\{1 + \lambda \exp\left[2\pi i\left(s + \frac{1}{2}\right)\phi\right]\right\}c_{s+1}^{\dagger}c_s + \text{H.c.}\right)\right.$$
$$\left. + \mu \sum_s \cos 2\pi s\phi c_s^{\dagger}c_s\right], \tag{1}$$

where ϕ corresponds to the magnetic flux per unit cell, and λ and μ are the nearest-neighbor hopping terms corresponding to each bond of the original 2D triangular lattice model. The phase diagram of the above 1D model in terms of the parameters λ and μ consists of two metallic phases and one insulating phase [19]. Here, we consider an alternative 2D lattice model consisting of a hexagonal lattice with anisotropic hopping in the presence of a perpendicular magnetic field. The anisotropic hexagonal model is given by [21,22]

$$H = -\sum_{n+m=\text{even}} [t_a c_{n,m+1}^{\dagger}c_{n,m} + t_b e^{-2\pi i(n+m)\phi}$$
$$\times c_{n+1,m}^{\dagger}c_{n,m} + t_c c_{n-1,m}^{\dagger}c_{n,m}] + \text{H.c.}, \tag{2}$$

where $c_{n,m}^{\dagger}$ ($c_{n,m}$) is the creation operator at site (n, m), and t_a, t_b, and t_c are the hopping amplitudes along the three different directions (see Fig. 13 in Appendix A), while 2ϕ is the magnetic flux enclosed per plaquette of the lattice. The phase factor associated with the magnetic flux ϕ is taken to be the inverse of the golden mean. This model yields an effective 1D model (for details see Appendix A) that also exhibits two metallic phases and one insulating phase; however, the phase diagram is completely different (see Fig. 1). The 1D model is given by

$$H_{\text{Harper}} = \sum_s \left(\Gamma_s^l c_{2s-1}^{\dagger} c_{2s} + \Gamma_s^r c_{2s+1}^{\dagger} c_{2s} + \text{H.c.} \right), \quad (3)$$

where the left and the right hopping parameters are given by $\Gamma_s^l = -t_a e^{ik_x} - t_b e^{ik_y + i4\pi s\phi}$ and $\Gamma_s^r = -t_c e^{ik_x}$, respectively. The operator $c_s^{\dagger}/c_s$ represents the creation/annihilation operator at site s, respectively. Note that while the GHM given by Eq. (1) involves quasiperiodicity in both the hopping and on-site term, the HH model has no on-site term while the quasiperiodicity is present in the hopping term.

In the earlier study [22], the phase diagram of this model was characterized by the fidelity, fidelity susceptibility, and VNE. It was shown that the fidelity and fidelity susceptibility acquire maximum value at the critical regions characterizing the phase boundaries or critical lines; on the other hand the rescaled VNE approaches unity in the metallic phase while it vanishes in the insulating phase. Here, as a complementary approach we utilize the inverse participation ratio (IPR) in order to characterize the phase diagram of this 1D Harper model, and it is defined as

$$IPR_n = \sum_{i=1}^{L} |\psi_n(i)|^4, \quad (4)$$

where $|\psi_n\rangle$ is the nth normalized single-particle eigenstate. In the delocalized regime, $IPR_n \propto L^{-1}$, and in the localized regime, $IPR_n \propto L^0$. We computed the IPR averaged over all eigenstates as a function of t_b/t_c and t_a/t_c while taking $t_c = 1$. The interplay between t_a and t_b results in a rich phase diagram consisting of two metallic phases separated by a critical line and an insulating phase. The metallic phases and insulating phase are separated from each other by the critical lines. The critical lines meet at the point $(t_a, t_b) = (1, 1)$, known as the bicritical point of this system shown in Fig. 1. In contrast to our model, which requires both parameters to be nonzero in order for a phase transition to occur, for the triangular lattice model, it is adequate to increase one parameter while maintaining the other at zero to trigger a phase transition [19,22].

III. SINGLE-PARTICLE DYNAMICS IN THE CRITICAL REGIONS

The spreading of a single-particle wave packet in quasiperiodic models has been studied extensively near the critical point [10,12,39–41]. In such scenarios, the probability distribution of the particle deviates from the Gaussian distribution resulting in anomalous diffusion. In previous works involving the single-particle cases, the focus of attention has been on the survival probability, the

density-density correlator, and the spreading of the wave packet via the second moment. In this section, we focus our attention on the analysis of the transport behavior via single-particle dynamics in the critical regions for the HH model. We consider the bicritical point and the critical lines and focus on the single-particle dynamics via the cross correlation $\langle c_x^{\dagger} c_{L/2} \rangle$ as well as the diagonal correlation $\langle c_x^{\dagger} c_x \rangle$.

For this purpose, we consider a system of length L with open boundary conditions and an initial state $|00\ldots01_{L/2}0\ldots0\rangle$, i.e., a single particle localized at the center of the lattice system. For this initial state, the two-point correlator is given by

$$C_{i,j} = \begin{cases} 1, & \text{if } i = j = L/2, \\ 0, & \text{otherwise.} \end{cases}$$

The probability to find a particle at time t is given by $P(x, t) = |\psi(x, t)|^2 = \langle c_x^{\dagger}(t) c_x(t) \rangle$, which can be calculated as follows,

$$\langle c_x^{\dagger}(t) c_y(t) \rangle = \sum_{k,j,l,m} [U^{\dagger}]_{jk} U_{kx} U_{lm} [U^{\dagger}]_{ym} e^{i(\epsilon_k - \epsilon_l)t}$$
$$\times \langle c_j^{\dagger}(0) c_m(0) \rangle,$$

where $U_{kx} = \langle k|x \rangle$ and ϵ_k is the eigenvalue of H for the kth single-particle eigenstate $|k\rangle$.

We find that the spatial profile of the wave packet broadens over time, with a power-law decay of the tail. Furthermore, we notice enhanced wave packet spread at the bicritical point as compared to the other critical regions. In addition, we observe that the cross correlation decays slower at the critical lines compared to the bicritical point, a behavior consistent with the above consideration. The cross correlation and the diagonal correlation at the critical regions exhibit the following scaling law,

$$\langle c_x^{\dagger}(t) c_x(t) \rangle \text{ or } \langle c_x^{\dagger}(t) c_{L/2}(t) \rangle \sim t^{-\alpha} f(x/t^{\alpha}). \quad (5)$$

From Figs. 2 and 3, we find that the wave packet spreading is superdiffusive in nature. We notice that at the bicritical point, the wave packet spreads with the scaling exponent $\alpha \approx 0.72$, while on the critical lines $\alpha \approx 0.65$ (as shown in Figs. 2 and 3 for the cross and the diagonal correlations, respectively). The spread of correlation allows us to distinguish the bicritical point from the other critical regions. The distinct nature of the bicritical point is consistent with the earlier studies where the spectral features of the bicritical point characterized via level spacing were found to be different as compared to those from the other critical regions [19,20,22]. Interestingly, we find that superdiffusive transport in the critical regions of the 1D HH model is faster than the superdiffusive transport at the critical point of the AAH model which has the scaling exponent $\alpha \approx 0.55$ [12].

IV. METALLIC PHASE CHARACTERIZATION VIA THE DW DYNAMICS

A. Initial DW setup via the multiparticle states

To study the nonequilibrium dynamics, we set up the initial DW profiles constructed via the multiparticle states rather than the GSA. In particular, we have considered two types of exotic multiparticle states; the first one is the GSG state as defined by Ghosh *et al.* [26], the second the entangled state as considered
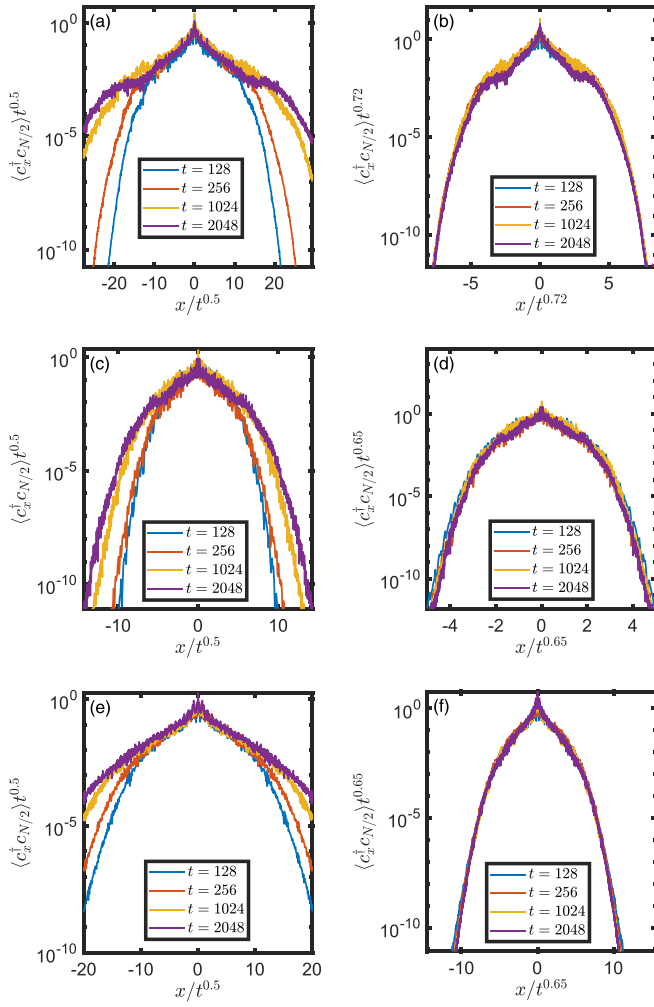
FIG. 2. For the isolated system case, the rescaled cross correlations $\langle c_x^\dagger(t) c_{L/2}(t) \rangle$ have been plotted as a function of position for the different times in the three different critical regions, which clearly deviates from the Gaussian distribution in all the above scenarios. The cross correlations scale with the exponent $\alpha \approx 0.72$ at the bicritical point $(1,1)$, as shown in (a), (b). For the critical line separating two metallic phases $(0.25, 0.25)$ in (c), (d) and for the critical line separating metallic and insulating phase $(1,10)$ in (e), (f) the scaling exponent turns out to be $\alpha \approx 0.65$. $L = 4501$.
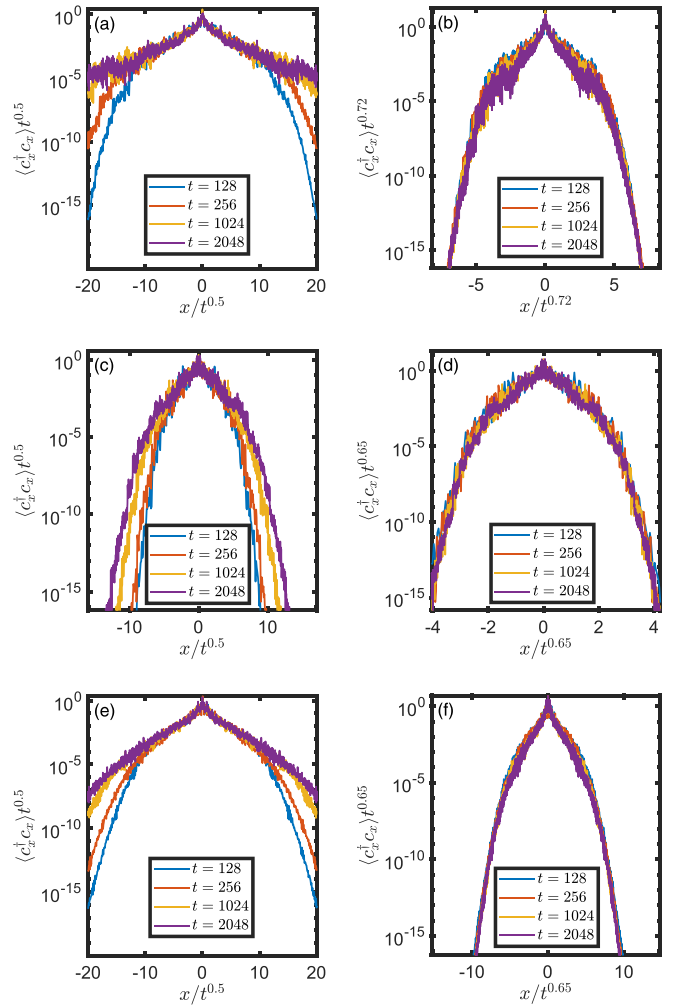
FIG. 3. For the isolated scenario, the rescaled diagonal correlations $\langle c_x^\dagger(t) c_x(t) \rangle$ with positions have been plotted for different times in the three critical regimes and similarly to the cross correlation, the diagonal correlation deviates from the Gaussian behavior in the critical regions. The diagonal correlation follows the power-law behavior with the scaling exponent $\alpha \approx 0.72$ in (a), (b) at the bicritical point $(1,1)$. For the critical line separating two metallic phases $(0.25, 0.25)$ in (c), (d) and at the critical line separating metallic and insulating phase $(1,10)$ for (e), (f), the power-law scaling exponent is $\alpha \approx 0.65$. $L = 4501$.

by Jin *et al.* [27]. Typically, the DW studies in the past was performed via the ground state approach in the clean system scenario where the DW state was prepared by considering the system in the ground state for the left and the right half of the system separately for a fixed particle density [30]. However, for the quasiperiodic scenario, the GSA only works for the DW state having one half of the chain fully filled while the other half empty. The GSA fails to create the other nontrivial DW setups involving one side partially filled and the other side empty for quasiperiodic systems (see Appendix B for further details).

First, we consider the GSG state which is defined by [26]

$$|\Psi_1\rangle = \prod_{l=1}^{L} \beta_l e^{\lambda_l c_l^\dagger} |0\rangle, \qquad (6)$$

where L is the total system size, $\lambda_l = \alpha_l e^{-i\phi_l}/\beta_l$ (α_l and β_l being real), and ϕ_l is phase at each site. The state is normalized by setting $\alpha_l^2 + \beta_l^2 = 1$. Moreover, one can manipulate the occupation at each site by tuning α_l and β_l such that $\alpha_l^2 - \beta_l^2 = 2m_l$ where $m_l = \langle c_l^\dagger c_l \rangle - 0.5$ and $\langle c_l^\dagger c_l \rangle$ is the occupation probability at the lth site. For this product state the two-point correlation matrix elements $C_{ij} = \langle \Psi | c_i^\dagger c_j | \Psi \rangle$ are given by

$$C_{i,j} = \begin{cases} \alpha_i^2, & \text{if } i = j, \\ \alpha_i \beta_i \alpha_j \beta_j e^{i(\phi_i - \phi_j)} P_{ij}, & \text{if } i \neq j, \end{cases}$$

where P_{ij} (for $|i - j| > 1$) is given by

$$P_{ij} = \prod_{k=\min\{i,j\}+1}^{\max\{i,j\}+1} \left(\beta_k^2 - \alpha_k^2 \right). \qquad (7)$$

By setting $\phi_l = 0$, we obtain $\lambda_l = \frac{\alpha_l}{\beta_l}$ and the multiparticle state becomes

$$|\psi_1\rangle = \prod_l (\beta_l |0\rangle + \alpha_l |1\rangle); \qquad (8)$$

therefore, at each site l the occupancy probability can be controlled by α_l. The GSG state provides the flexibility to control the occupation at each site. For $\alpha_l = 1$ and $\beta_l = 0$, we have the fully filled state $|111\ldots1\rangle$. A more complicated state, such as the Néel state $|1010\ldots\rangle$, is obtained by setting $\alpha_{2l-1} = 1$, $\alpha_{2l} = 0$, and $\beta_l = 0$. Also one can form a DW state for filling fraction α_l^2 where $l < L$ (full length of the system).

The second type of multiparticle state that we consider is a spatially entangled state expressed in terms of two parameters, n_d the particle density and l_c the number of sites over which the coherence length is maintained [27]. The state can be written as

$$|\psi\rangle = \frac{1}{\sqrt{\binom{l_c}{n_d l_c}}} \sum_l |\phi_l\rangle, \qquad (9)$$

where $l = 1, 2, \ldots \binom{l_c}{n_d l_c}$. The elements of the (two-point) correlation matrix are given by

$$C_{m,n} = \begin{cases} n_d, & \text{if } m = n, \\ \frac{l_c - |m-n|}{l_c} c_{1,1+|m-n|}^{l_c}, & \text{if } m \neq n, \ |m-n| \leqslant l_c, \\ & \text{and } m, n \leqslant L, \\ 0, & \text{otherwise}, \end{cases}$$

where $c_{j,k}^{l_c} = \text{tr}[\rho c_j^\dagger c_k]$ is the two-point correlation of the subsystem of length l_c, and $\rho = |\psi\rangle\langle\psi|$.

Here we are considering the single particle to be spread over the l_c sites; i.e., the density $n_d = 1/l_c$ and the entangled state for each particle can be expressed as follows,

$$|\psi\rangle = \frac{1}{\sqrt{l_c}} \sum_{k=1}^{l_c} c_k^\dagger |0\rangle. \qquad (10)$$

Correspondingly, $c_{j,k}^{l_c}$ is given by

$$c_{i,j}^{l_c} = 1/l_c \text{ for all } i, j, \qquad (11)$$

and total wave function is given by

$$|\Psi_2\rangle = \prod_{i=1} |\psi_i\rangle. \qquad (12)$$

By this multiparticle state one can control the particle density via the coherence length. In Appendixes C and D we study the dynamics corresponding to this state.

B. DW dynamics via the GSG state approach

The metallic and insulating phases, as well as the critical regions in the phase diagram of the extended Harper model, have been characterized in the literature with the help of multiple techniques, for example the fidelity susceptibility, von Neumann entropy, and multifractal analysis, all of which are complementary analyses [20,22,24,25]. However, the aforementioned methodologies do not distinguish the two
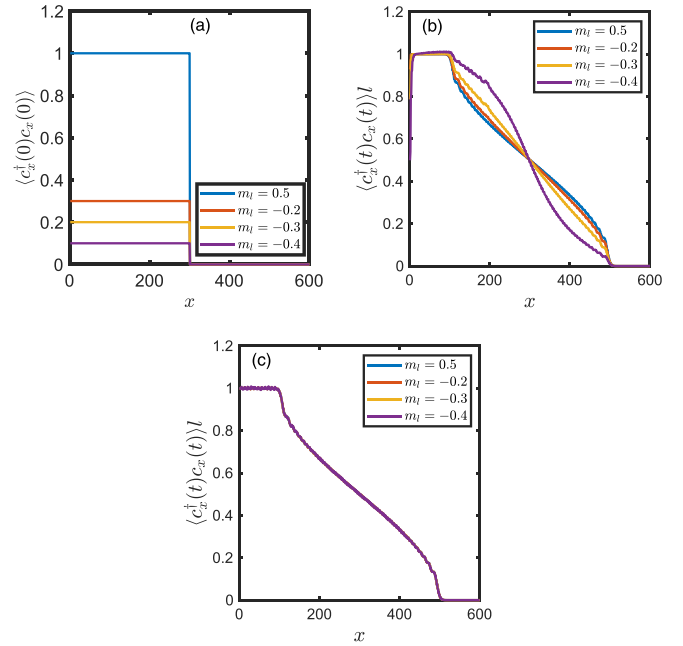

FIG. 4. Here, the domain wall melting has been plotted in the deep metallic regime of both metallic phases at time $t = 100$ for system size $L = 600$. (a) The initial domain wall state is prepared for different particle density ($\langle c_x^\dagger c_x \rangle = m_l + 0.5$) at the left half while the right half being empty. (b) The front profile of the rescaled density exhibits the initial density dependence in MP1 (10, 0.005). (c) For MP2 (0.005,10), the rescaled density front for different initial density propagates with the same front profile.

metallic phases [22]. As an alternate approach, we study the DW dynamics in the metallic regimes. We consider two types of DW state. The first one is the uncorrelated DW state, in which half of the chain is entirely filled, and the remaining region is empty. The second scenario involves a correlated DW state with partial filling in one half while the other half is empty. Interestingly, we find that the dynamics of the uncorrelated DW state is the same for both the metallic phases; however the dynamics corresponding to the correlated DW state exhibits different behavior in the two metallic regimes.

We begin by studying the rescaled density in the two metallic phases with a particular focus on the deep metallic regimes, i.e., $t_b \ll 1$ for metallic phase 1 (MP1) and $t_a \ll 1$ for metallic phase 2 (MP2). In both the metallic phases the front propagation speed is the same; however, the shape of the rescaled density front for the correlated DW state is different (see Fig. 4). The rescaled density profile of the correlated DW state exhibits the initial DW height dependence in MP1 [see Fig. 4(b)] while this remains absent in MP2 [Fig. 4(c)]. However, the uncorrelated DW state exhibits the same dynamics in both the metallic phases. For the correlated DW state, the correlation in the initial state constrains the dynamics in MP1 and results in a distinct particle density profile [27], while in MP2 the effect of correlation is not there.

Next, we investigate the transport dynamics in all regimes of the phase diagram via the total number of transferred
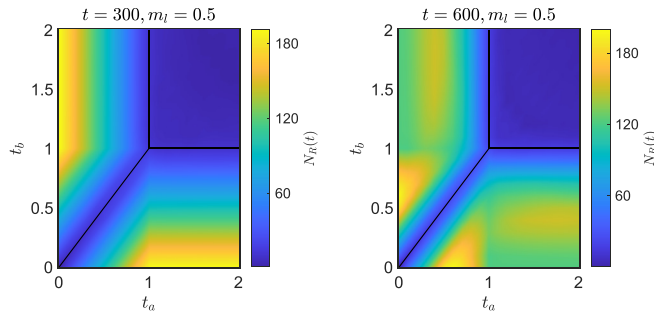
FIG. 5. For the fully filled DW constructed by the initial GSG state, the total number of transferred particles $N_R(t)$ as a function of t_a and t_b for different times t has been plotted. $L = 600$.

particles, N_R, from the left to the right half,

$$\langle \hat{N}_R(t) \rangle = \sum_{x=L/2}^{L} \langle c_x^{\dagger}(t) c_x(t) \rangle. \tag{13}$$

For this analysis we first consider a fully filled DW state and find that the total number of transferred particles is equal in both the metallic regimes as plotted in Fig. 5. Similarly to the front propagation studies, the distinction between the two metallic phases is revealed by considering the partially filled DW state. In particular, we find that the rate of transfer of particles is different in the two metallic regimes as shown in Fig. 6.

The total number of transferred particles $N_R(t)$ at small time in the deep metallic phase exhibits linear growth with respect to time (Fig. 7), i.e.,

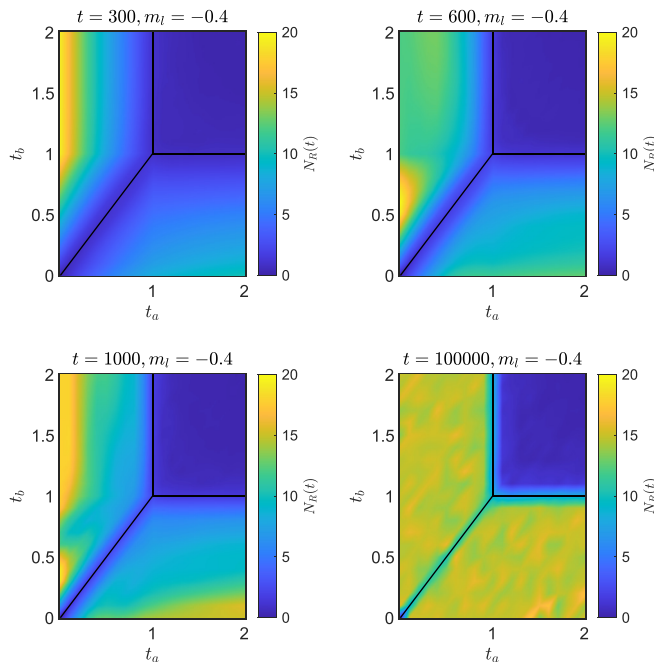$$N_R(t) \propto t\nu^{\alpha}, \tag{14}$$

FIG. 6. The total number of transferred particles $N_R(t)$ as a function of t_a and t_b for different times t has been plotted for the partially filled DW state made by the initial GSG state. $L = 600$.
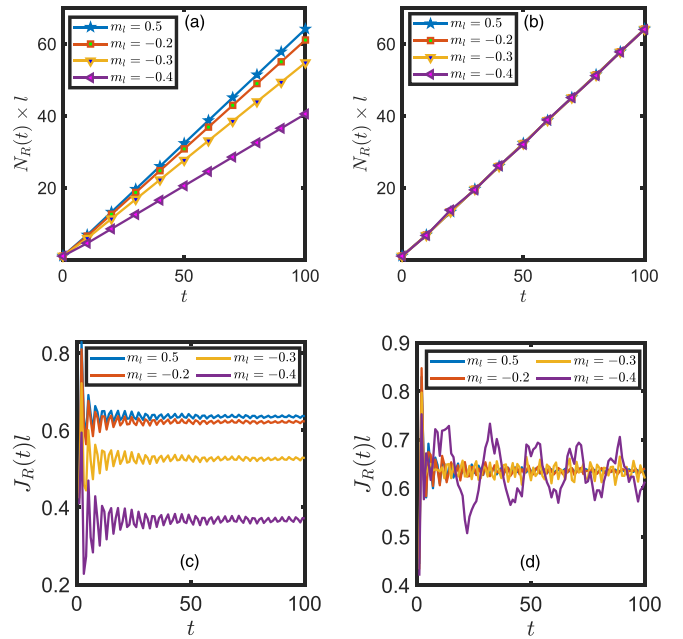

FIG. 7. Here, we have plotted the rescaled total number of transferred particles ($N_R \times l$) and the rescaled particle current ($J_R \times l$) as a function of time t for the different particle densities (m_l) for metallic phase 1 (10, 0.005) in (a) and (c) and for metallic phase 2 (0.005, 10) in (b) and (d).

where $\nu = \langle c_x^{\dagger}(0) c_x(0) \rangle = 1/l$ is the initial filling fraction, and $\alpha = 1$ for both MP1 and MP2; the difference is that while for MP1 the proportionality constant depends on the filling fraction, it is independent for MP2 [see Figs. 7(a), 7(b)]. Furthermore, we find that MP1 has a lower total number of transferred particles than MP2. Figures 7(c) and 7(d) show that the DW height dependence is also seen in the rescaled current in MP1, but not in MP2. In addition, we observe that in MP2 compared to MP1, the transient current has larger amplitude. We obtain similar results involving distinct dynamics of MP1 and MP2 (see Appendix C) for a different type of entangled state other than the GSG state.

Thus both the GSG and the entangled states are able to distinguish the two metallic phases. Moreover, we find that the transport behavior of the MP1 of the HH model is similar to the transport in the metallic phase of the AAH model, as shown in Appendix D.

V. THE NESS TRANSPORT FOR THE OPEN SYSTEM

In earlier studies on the open quantum system involving the AAH model it was established that the NESS transport at the critical point exhibits anomalous diffusive behavior [11,12]. Here we determine that the transport scaling exponents in the critical regions of the 1D HH model correspond to subdiffusive transport however, the exponents differ from that of the AAH model.

We find that in the open scenario, unlike in the isolated scenario case, the DW transport behavior in the deep metallic regime of the two metallic phases is identical. In addition, we find an interesting even and odd system size dependence of the correlators $\langle c_j^{\dagger} c_j \rangle$ in both the metallic phases.

In an open system, the NESS transport can be characterized by the current, J, scaling with respect to the system size L, i.e., $J \sim L^{-\alpha}$. For $0 < \alpha < 1$, the transport is superdiffusive while for $\alpha > 1$, the transport is subdiffusive [42]. In the two limiting scenarios, $\alpha = 0$ and $\alpha = 1$, the transport is ballistic and diffusive, respectively. We utilize the Lindblad master equation (LME) formalism to study the NESS behavior of the two-point correlator of the system. The time evolution equation of the system density matrix $\rho_s(t)$ is given by the usual LME [6,11,17,43],

$$\frac{d\rho_s}{dt} = -i[H, \rho_s] + \mathcal{L}_1\rho_s + \mathcal{L}_L\rho_s, \qquad (15)$$

where the effect of the reservoir on the dynamics of the system is captured by $\mathcal{L}_i$, which is given by

$$\mathcal{L}_i\rho_s = \gamma(1 - f_i)\left(c_i\rho_s c_i^\dagger - \tfrac{1}{2}\{c_i^\dagger c_i, \rho_s\}\right)$$
$$+ \gamma f_i\left(c_i^\dagger \rho_s c_i - \tfrac{1}{2}\{c_i^\dagger c_i, \rho_s\}\right), \qquad (16)$$

where $i = 1, L$ and γ is the system-bath coupling parameter. The correlation matrix C at time t is given by

$$C_{ij}(t) = \langle c_i^\dagger(t)c_j(t) \rangle = \text{tr}[\rho_s(t)c_i^\dagger c_j], \qquad (17)$$

and we can obtain $C_{ij}(t)$ (see Appendix E) by solving the equation

$$\frac{dC}{dt} = -(TC + CT^\dagger) + P, \qquad (18)$$

where $T = iH + \frac{\gamma}{2}R$ with $R_{11} = R_{LL} = 1$, and $P_{11} = \gamma f_1, P_{LL} = \gamma f_L$, while all the other P_{ij} and R_{ij} vanish. For the steady state solution, Eq. (18) reduces to the Lyapunov equation,

$$TC + CT^\dagger = P. \qquad (19)$$

From the NESS correlation matrix, C, we obtain the form of the current operator as

$$J_{j,j+1} = i\tilde{\Gamma}_j(c_j^\dagger c_{j+1} - c_{j+1}^\dagger c_j)$$
$$= 2\text{Im}(\tilde{\Gamma}_j C_{j,j+1}), \qquad (20)$$

where $\tilde{\Gamma}_j$ is defined as

$$\tilde{\Gamma}_j = \begin{cases} t_a e^{ik_x} + t_b e^{ik_y + i4\pi j\phi}, & j = \text{odd}, \\ t_c e^{-ik_x}, & j = \text{even}, \end{cases}$$

and the correlation term $C_{j,j+1} = \langle c_j^\dagger c_{j+1} \rangle$.

The current scaling with the system size for different phases is plotted in Fig. 8. In the metallic regime the transport is ballistic, i.e., $J \sim L^0$, while the current in the insulating regime decreases exponentially with the system size, i.e., $J \sim e^{-L}$. Interestingly, unlike the isolated scenario, here we find that the scaling exponents for the current at the critical point and the critical lines are identical ($\alpha \approx 1.26$), which is however different from the open system transport scaling exponent at the critical point of the AAH model ($\alpha \approx 1.4$) [12].

In addition, we have studied the effect of the system-bath coupling parameter, γ, on the steady state current. We find that in the deep metallic regime there is an unusual even-odd size effect on the steady state current. Interestingly, we find that for odd system size the maximum current in MP2
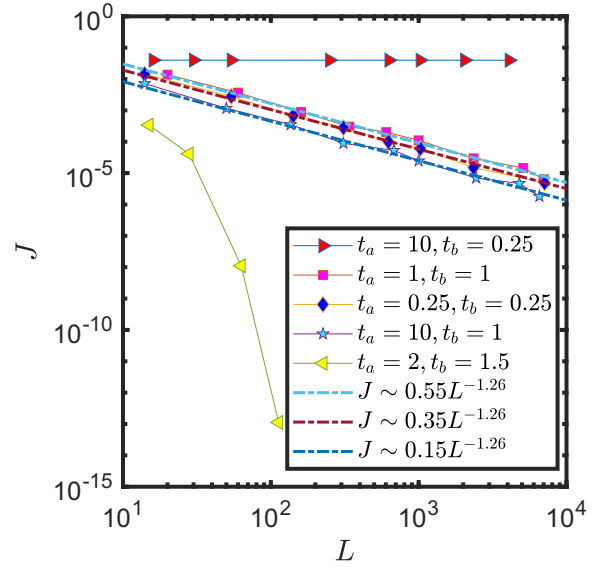

FIG. 8. NESS current (J) as a function of system size (L) has been plotted for different phases. Here, $t_a = 10, t_b = 0.25$ is for the insulating phase, $t_a = 1 = t_b$ is the bicritical point, $t_a = 0.25 = t_b$ is on the metal-1-metal-2 critical line, $t_a = 10, t_b = 1$ is on the metal-insulator transition line (setting $\phi = \frac{\sqrt{5}-1}{2}, \gamma = 1$).

(MP1) turns out to be independent of t_b (t_a), while the corresponding optimal values of the system-bath couplings exhibit linear dependence on the hopping parameter, $\gamma_{\text{opt}} \propto t_b$ in MP2 (t_a in MP1) as shown in Fig. 9(a). On the other hand, for the even system size in MP2 (MP1), the maximum current, $J_{\max} \propto \frac{1}{t_b}$ ($J_{\max} \propto \frac{1}{t_a}$), is reached at the bath coupling parameter $\gamma_{\text{opt}} \approx 2$ [see Fig. 9(b)]. Furthermore, we find that for the large system-bath coupling parameter, i.e., $\gamma > \gamma_{\text{opt}}$, the current exhibits power-law suppression with respect to the coupling parameter, $J \propto \gamma^{-1}$. In the other limit, $\gamma < \gamma_{\text{opt}}$, the NESS current grows linearly with the system-bath coupling; i.e., $J \propto \gamma$ for both the even and odd system sizes. To characterize the behavior of the local density, we have plotted the NESS particle density for a specific site in Fig. 10 and particle density profile for different phases in Fig. 11. While in the insulating phase, localization implies strongly suppressed flow of particle density [see Fig. 11(a)], in the critical regions, the particle density decreases continuously from one side to the other [see Fig. 11(b)]. In the metallic regime, we again find odd-even system size dependence of the particle density. For the even system size we find that the particle density fluctuates around $\langle c_x^\dagger c_x \rangle = 0.5$, with the fluctuations suppressed deep in the metallic regime as can be seen from Fig. 11(c). The fluctuations are suppressed with the decrease of parameter t_a deep in the metallic regime. Furthermore, for the even system size scenario, we find that the particle density remains constant for the different t_b values which is shown for the deep metallic regime of the metallic phase 2 [see the inset Fig. 11(c)]. On the other hand, for the odd system size, the particle density fluctuation is suppressed again by the t_a parameter which can be seen from Fig. 11(d); however, the particle density value increases with the increase of the t_b parameter value and reaches the maximum value $\langle c_x^\dagger c_x \rangle = 1$ shown in the inset of Fig. 11(d). This emerging
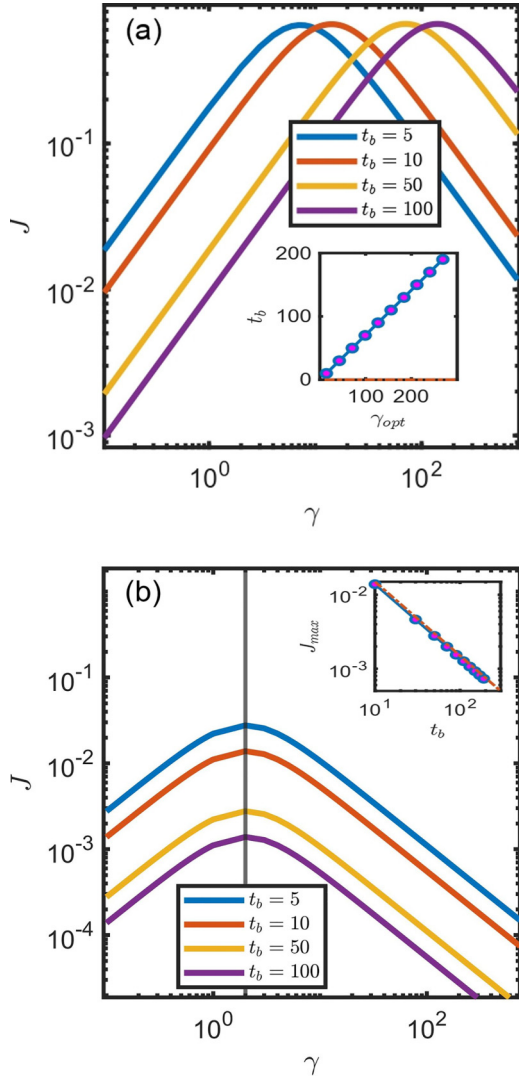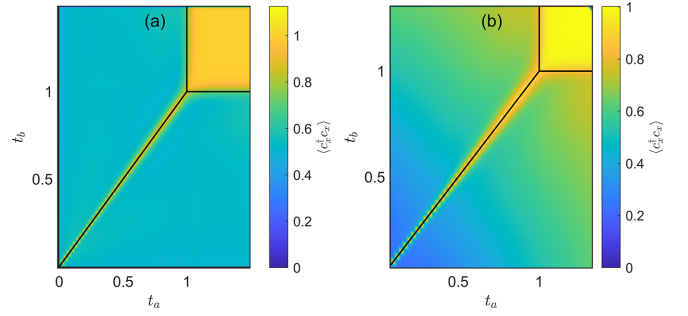
FIG. 10. The NESS local particle density has been plotted as a function of parameters t_a and t_b for (a) $L = 150$ considering the even system size, and (b) $L = 151$ for the odd system size, respectively. Here, we have fixed the site index $x = 30$ and the parameter $\gamma = 1$.

VI. SUMMARY

In the present work, we have studied various aspects of the transport phenomena in the HH model for isolated and open system scenarios. For the isolated case, the cross correlation and diagonal correlation exhibit nonuniversal scaling laws with exponents in the critical regions different from those obtained for the AAH model. By considering the single-particle dynamics we show that the two-point correlation has a faster spread at the bicritical point compared to the other critical regions.

FIG. 9. In the deep regime of MP2 where $t_a = 0.005$, the NESS current as a function of the system-bath coupling parameter has been plotted for the odd and even system size. (a) For the odd system size ($L = 151$), the maximum current for different points in the metallic regime is obtained at the different optimal system-bath coupling values. The linear dependence of optimal system-bath coupling as a function of t_b parameter has been shown in the inset. (b) For the even system size ($L = 150$), the NESS current for different t_b parameter values becomes maximum at a constant system-bath coupling parameter and the inset depicts the maximum current's linear dependence with t_b.

even-odd effect can be understood by taking into account the inherent structure of the Hamiltonian composed of alternating bonds, Γ^l and Γ^r, which couples with the bath asymmetrically or symmetrically depending upon the odd or even number of sites, respectively (see Fig. 12). As a result of symmetric coupling (i.e., the end bonds are the same), the average NESS density for the even system size takes the value of the mean of the two baths while for the odd system size due to the asymmetric coupling the strength of the hopping plays a crucial role. In the limit $t_b \gg t_c$ ($t_b \ll t_c$), the left (right) bath density controls the average NESS density in the wire fully as shown in Fig. 11(d).
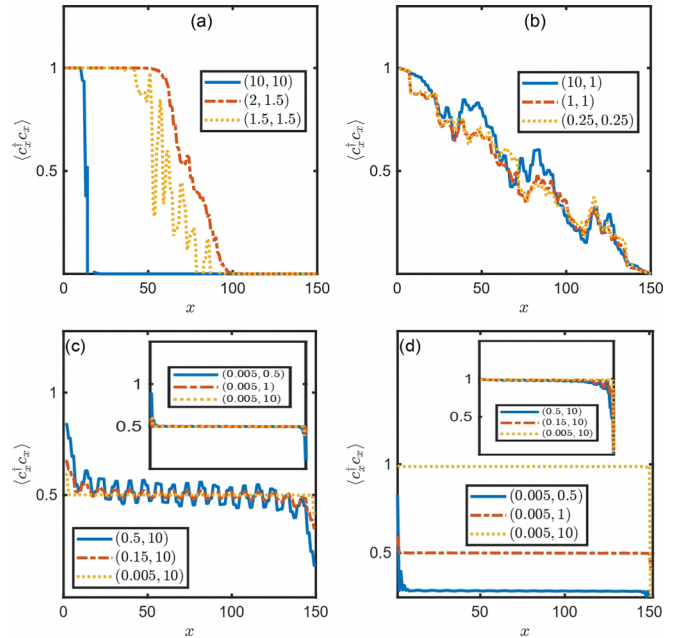

FIG. 11. The particle density profile in the NESS is shown in the different phases. (a) NESS density for different t_a and t_b values in the insulating regime, (b) at the metal-insulator transition line ($t_a = 10, t_b = 1$), at the bicritical point ($t_a = 1, t_b = 1$), and at the metal-metal critical line ($t_a = 0.25, t_b = 0.25$). The local density has been plotted in metallic phase 2 with the constant t_b parameter for the even ($L = 150$) and odd ($L = 151$) system size in (c) and (d), respectively, where in the inset of (c) and (d) we consider the local density for the constant t_a parameter ($\gamma = 1$).
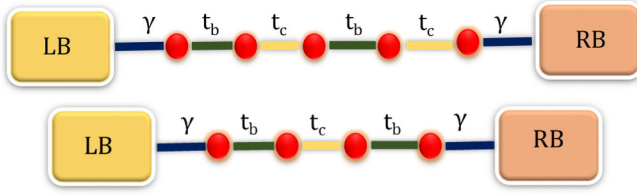
FIG. 12. Schematic diagram of the system coupling with the bath for an even and odd system size and the system Hamiltonian is considered for the deep metallic regime of MP2. For an odd system size, the system couples with bath asymmetrically, while for the even system size, the system couples symmetrically with the bath.

FIG. 13. Visualization of hexagonal Harper model through brick wall geometry.

One of the most important aspects of our study in the isolated system scenario is the establishment of a clear distinction between the two metallic phases by utilizing exotic initial states for preparing the system in an inhomogeneous DW state. In particular, we have obtained a scaling law for the total number of transferred particles while tracking the dynamics of the system from an initial domain wall (DW) state constructed via the GSG state and the entangled state. We find that for low filling fraction, the transport behavior for both the GSG state and the entangled state case are different in the deep metallic regimes of the MP1 and MP2. Our approach provides an alternative to study such phases from the transport perspective.

In the open system scenario, the current in the NESS exhibits subdiffusive transport along the critical lines and at the bicritical point. We find that unlike the transport in the isolated scenario, the open system transport has the same scaling exponent for the different critical regions. Interestingly, the transport exhibits an unusual even-odd effect on the system size. For the even system size the maximum current is found at a fixed system-bath coupling, $\gamma_{opt} \approx 2t_c$, while for the odd system size, the maximum current varies with the optimal system-bath coupling $\gamma_{opt} \propto t_b$ (t_a) for MP2 (MP1). Moreover transport is found to be identical in the two metallic phases for the open system scenario.

We also analyzed the NESS density in different phases. The density profile exhibits completely different behavior in the metallic, insulating, and critical regions. Interestingly, the MP1-MP2 transition line exhibits a density profile similar to the critical phase density profile; however, the two metallic phases do not exhibit any distinct behavior, unlike the isolated system. We have also studied the dynamics along the MP1-MP2 transition line in this work, which has not been previously reported. The analysis of the transport phenomena in the MP1-MP2 critical line is identical to that of the metal-insulator transition line in both of the scenarios considering the isolated and the open system. The above analysis of the present study sheds light on the intricate transport behavior of the 1D HH model characterizing the distinct phases and their dynamics. Similar transport behavior can be expected from the triangular lattice model [Eq. (1)]. Experimentally such a model can be realized in the ultracold atoms and photonic lattice setup [44–48] where our results can be verified.
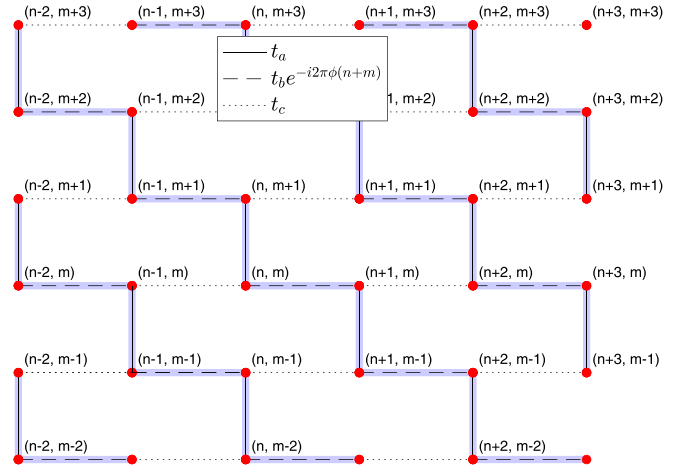
APPENDIX A: 1D HEXAGONAL HARPER HAMILTONIAN

The Hamiltonian of the 2D hexagonal model is given by

$$H = -\sum_{m+n=even} [t_b e^{-i2\pi\phi(m+n)} c_{n+1,m}^\dagger c_{n,m}$$
$$+ t_a c_{n,m+1}^\dagger c_{n,m} + t_c c_{n-1,m}^\dagger c_{n,m}] + \text{H.c.} \quad (A1)$$

For a visual representation of the translational invariance present in the model, it is convenient to use the brick wall geometry as shown in Fig. 13. Consider the eigenstate of H expressed in the following form,

$$|\psi\rangle = \sum_{n',m'} A_{n',m'} c_{n',m'}^\dagger |0\rangle. \quad (A2)$$

Plugging it into the eigenvalue equation and rearranging terms we obtain

$$E|\psi\rangle = -\sum_{m+n=even} \left(t_b e^{i2\pi\phi(m+n)} A_{n+1,m} + t_a A_{n,m+1} \right.$$
$$+ t_c A_{n-1,m}) c_{n,m}^\dagger |0\rangle - \sum_{m+n=odd} (t_b e^{-i2\pi\phi(m+n-1)} A_{n-1,m}$$
$$\left. + t_a A_{n,m-1} + t_c A_{n+1,m} \right) c_{n,m}^\dagger |0\rangle. \quad (A3)$$

We reparametrize the indices in terms of the new indices $s = -(m+n)$ and $d = m - n$ with $A_{n,m} \to \mathcal{A}_{s,d}$. Comparing the coefficients for even s we obtain

$$E\mathcal{A}_{s,d} = -(t_b e^{-i2\pi\phi s} \mathcal{A}_{s-1,d-1} + t_a \mathcal{A}_{s-1,d+1} + t_c \mathcal{A}_{s+1,d+1}). \quad (A4)$$

We next define $\tilde{\mathcal{A}}_{s,k_d} = \sum_d e^{ik_d d} \mathcal{A}_{s,d}$, where $k_d = (k_x - k_y)/2$. The above equation thus reduces to the following form,

$$E\tilde{\mathcal{A}}_{s,k_d} = -[(t_b e^{-i2\pi\phi s+ik_d} + t_a e^{-ik_d})\tilde{\mathcal{A}}_{s-1,k_d}$$
$$+ t_c e^{-ik_d} \tilde{\mathcal{A}}_{s+1,k_d}]. \quad (A5)$$

Similarly, comparing the coefficients for odd s and expressing the equation in the momentum space yields

$$E\tilde{\mathcal{A}}_{s,k_d} = -[(t_b e^{i2\pi\phi(s+1)-ik_d} + t_a e^{ik_d})\tilde{\mathcal{A}}_{s+1,k_d}$$
$$+ t_c e^{ik_d}\tilde{\mathcal{A}}_{s-1,k_d}]. \quad (A6)$$

Corresponding to the equations (A5) and (A6), the following effective 1D Hamiltonian can be constructed for each of the k_d modes,

$$H_{\text{Harper}} = \sum_{s=even} [(-t_b e^{i2\pi\phi s-ik_d} - t_a e^{ik_d})c_{s-1}^\dagger c_s$$
$$- t_c e^{ik_d}c_{s+1}^\dagger c_s] + \text{H.c.} \quad (A7)$$

$$= \sum_s [(-t_b e^{i4\pi\phi s-ik_d} - t_a e^{ik_d})c_{2s-1}^\dagger c_{2s}$$
$$- t_c e^{ik_d}c_{2s+1}^\dagger c_{2s}] + \text{H.c.} \quad (A8)$$

The Hamiltonian given in Eq. (A8) is an equivalent 1D effective Hamiltonian of the hexagonal Harper model which yields all the results discussed in the paper. To bring it to the specific form used in Refs. [22,23], we perform the following gauge transformation: $c_{2s} \rightarrow e^{ik_x/2}c_{2s}$ and $c_{2s\pm1} \rightarrow e^{-ik_y/2}c_{2s\pm1}$ (here we have considered the open boundary condition). This transformation yields Eq. (3) which is used in the main text:

$$H = \sum_s [(-t_b e^{i4\pi\phi s+ik_y} - t_a e^{ik_x})c_{2s-1}^\dagger c_{2s}$$
$$- t_c e^{ik_x}c_{2s+1}^\dagger c_{2s}] + \text{H.c.} \quad (A9)$$

APPENDIX B: FAILURE IN CREATING AN INITIAL CLEAN DW STATE VIA THE GSA

The ground state of the 1D HH model of length L with (average) filling fraction $\frac{n}{L}$ can be written as $|\Psi_{\text{GS}}^n\rangle = \Pi_{k=1}^n a_k^\dagger |0\rangle$, where $a_k^\dagger$ creates a fermionic state in kth lowest-energy state of the single-particle eigenvalue spectrum [29]. There is no site-dependent control over the filling in GSA. As can be seen from Fig. 14, only a fully filled DW can be constructed perfectly in any of the metallic regimes considering the HH model (a quasiperiodic system). Moreover, we cannot obtain perfect/clean DW for a partial filling fraction in the HH model as shown in Fig. 14; i.e., there are abrupt fluctuations of the initial particle density due to the quasiperiodicity of the hopping parameters.

APPENDIX C: DW DYNAMICS CONSIDERING THE ENTANGLED STATE APPROACH

Here, we have analyzed the dynamics from the initial DW setup constructed via the entangled state as discussed in Sec. IV A. We clearly observe that the entangled state in the deep metallic regime exhibits a unique transport behavior similar to the GSG state (see Fig. 15). We have also plotted the particle density as a function of time in Fig. 16, which also exhibits exactly the same behavior as in the case of the DW dynamics initialized via the GSG state. The above analysis indicates that the DW dynamics of the HH model can be studied in general by considering these kinds of exotic initial multiparticle states, i.e., the GSG state or the
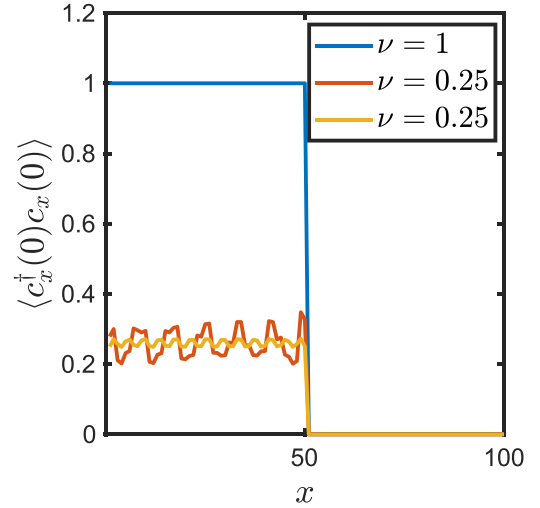

FIG. 14. The initial DW constructed by the GSA in the metallic regime of the HH model is plotted. The fully filled DW ($\nu = 1$) is shown for the parameters ($t_a = 10$, $t_b = 0.005$) while the partially filled ($\nu = 0.25$) DW has been plotted with colors orange and red for parameters ($t_a = 10$, $t_b = 0.005$) and ($t_a = 10$, $t_b = 0.25$), respectively. The initial DW profile exhibits strong fluctuations in the partially filled case.

entangled state, and irrespective of the nature of the initial state we obtain the same dynamical behavior once the DW setup is successfully done. However, the GSA fails in creating the perfect initial DW state with partial fillings for the quasiperiodic systems, i.e., the AAH and the HH model in general.
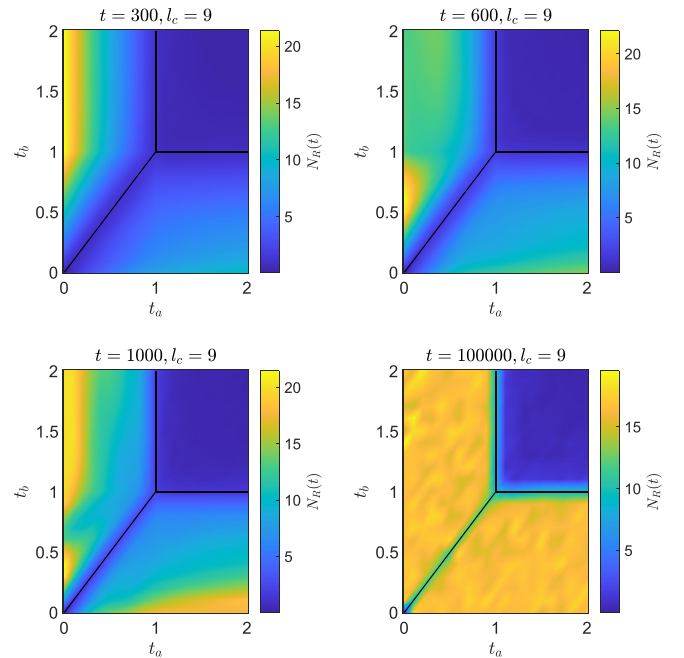

FIG. 15. The total number of transferred particles $N_R(t)$ as a function of parameters t_a and t_b has been plotted for the different times t considering the DW dynamics initiated by the entangled state approach (by setting $L = 600$).
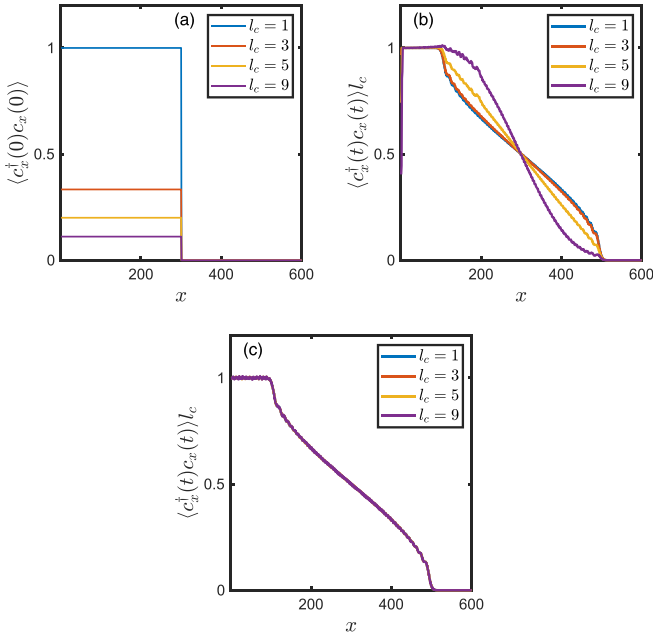
FIG. 16. The rescaled particle density spread has been shown for the entangled DW state. (a) Here, the initial DW state for different coherence length has been plotted, where the right side is filled and left side is empty. (b) For MP1, the DW front profile exhibits the coherence length dependence which is associated with the particle density. (c) For MP2, the DW with different coherence length propagates with the same profile.

APPENDIX D: DW DYNAMICS IN AAH MODEL VIA THE ENTANGLED STATE APPROACH

We have also studied the DW dynamics for the case of the AAH model by considering the entangled state approach for the initial state preparation. We observe that the metallic phase of the AAH model exhibits a behavior similar to the MP1 as shown in Fig. 17, and in particular, the two-point correlator scales as

$$\langle c_m^\dagger(t)c_m(t)\rangle \propto \nu^\alpha, \tag{D1}$$

$$N_R(t) \propto \nu^\alpha, \tag{D2}$$

where $\alpha \neq 1$. Moreover, despite considering a disorder in the on-site term, it does not exhibit the behavior of the metallic phase 2 of the HH model.

APPENDIX E: LINDBLAD EQUATION

Considering the system with the Hamiltonian $H = \sum_{i,j} H_{ij} c_i^\dagger c_j$ connected with the bath at each site, the Lindblad equation describing the time evolution of the state of the system can be written as

$$\frac{d\rho_s}{dt} = -i[H, \rho_s] + \sum_i \mathcal{L}_i \rho_s, \tag{E1}$$

where the Lindbladian operator characterizing the dissipation process turns out to be the fermionic annihilation operator,
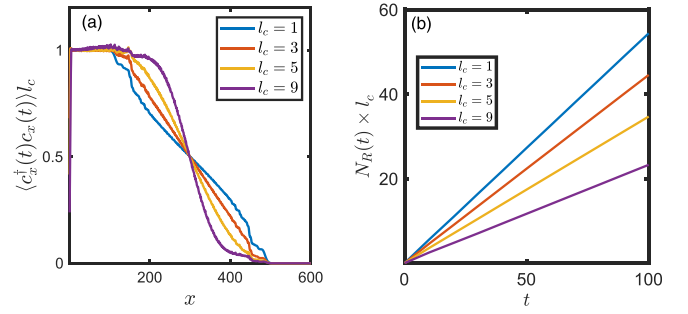

FIG. 17. Here, for the case of entangled DW state, the rescaled particle density profile at time $t = 100$ and the total number of transferred particles in the metallic phase of AAH model have been shown. In (a) the rescaled density profile exhibits the dependence on the initial density. (b) The total number of transferred particles as a function of time has been plotted. $\lambda = 0.15$, $L = 600$.

$L_i = c_i$; then,

$$\begin{aligned}\mathcal{L}_i \rho_s &= \gamma(1 - f_i)\big(c_i \rho_s c_i^\dagger - \tfrac{1}{2}\{c_i^\dagger c_i, \rho_s\}\big) \\ &\quad + \gamma f_i\big(c_i^\dagger \rho_s c_i - \tfrac{1}{2}\{c_i^\dagger c_i, \rho_s\}\big).\end{aligned} \tag{E2}$$

Next, the above equation can be divided into two parts as follows: $\mathcal{L}_i = \gamma(1 - f_i)\mathcal{L}_i^1 + \gamma f_i \mathcal{L}_i^2$. Furthermore, our goal is to calculate the two-point correlator, $C_{m,n}(t) = \langle c_m^\dagger(t) c_n(t)\rangle$. Next, we would like to utilize some basic identities given by

$$\mathrm{tr}[A, B]C = -\mathrm{tr}B[A, C], \tag{E3}$$

$$[c_i^\dagger c_j, c_k] = -\delta_{ik} c_j, \tag{E4}$$

$$[c_i^\dagger c_j, c_k^\dagger] = \delta_{jk} c_i, \tag{E5}$$

in calculating the $C_{m,n}(t)$. The time evolution of $C_{mn}(t)$ is given by

$$\begin{aligned}\frac{d}{dt}C_{m,n}(t) &= \frac{d}{dt}\mathrm{tr}[\rho_s(t)c_m^\dagger c_n] \\ &= \mathrm{tr}\left[\frac{\partial \rho_s}{\partial t}c_m^\dagger c_n\right].\end{aligned} \tag{E6}$$

Substituting Eq. (E1) in Eq. (E6) and using the above identities Eqs. (E3)–(E5), we obtain

$$\begin{aligned}\frac{d}{dt}C_{m,n}(t) &= \mathrm{tr}\left[-i[H, \rho_s]c_m^\dagger c_n + \sum_{i=1}^{L} \mathcal{L}_i \rho_s c_m^\dagger c_n\right] \\ &= i\langle[H, c_m^\dagger c_n]\rangle + \sum_{i=1}^{L}\langle \mathcal{L}_i c_m^\dagger c_n\rangle.\end{aligned} \tag{E7}$$

Upon simplifying the first term in Eq. (E7), we obtain

$$\begin{aligned}[H, c_m^\dagger c_n] &= \sum_{ij} H_{ij}[c_i^\dagger c_j, c_m^\dagger c_n] \\ &= -\sum_j H_{nj}c_m^\dagger c_j + \sum_i H_{im}c_i^\dagger c_n.\end{aligned}$$

Next, for calculating the $\mathcal{L}_i c_m^\dagger c_n$, we simplify $\mathcal{L}_i^1(c_m^\dagger c_n)$ and $\mathcal{L}_i^2(c_m^\dagger c_n)$, which result in

$$
\begin{aligned}
\mathcal{L}_i^1(c_m^\dagger c_n) &= c_i(c_m^\dagger c_n)c_i^\dagger - \tfrac{1}{2}\{c_i^\dagger c_i, (c_m^\dagger c_n)\} \\
&= \tfrac{1}{2}c_i^\dagger[c_m^\dagger c_n, c_i] + \tfrac{1}{2}[c_i, c_m^\dagger c_n]c_i \\
&= -c_m^\dagger c_n \tfrac{1}{2}(\delta_{in} + \delta_{im})
\end{aligned}
\tag{E8}
$$

and

$$
\mathcal{L}_i^2(c_m^\dagger c_n) = c_n c_m^\dagger \tfrac{1}{2}(\delta_{in} + \delta_{im}).
\tag{E9}
$$

Then,

$$
\begin{aligned}
\mathcal{L}_i c_m^\dagger c_n &= -\gamma_i(1 - f_i)\tfrac{1}{2}(\delta_{in} + \delta_{im})c_m^\dagger c_n \\
&\quad + \gamma_i f_i \tfrac{1}{2}(\delta_{in} + \delta_{im})c_n c_m^\dagger \\
&= -\frac{\gamma_i}{2}(\delta_{in} + \delta_{im})c_m^\dagger c_n + \gamma_i f_i \delta_{im}\delta_{mn}.
\end{aligned}
\tag{E10}
$$

Finally, by substituting all the above simplified terms in Eq. (E7), we obtain

$$
\frac{d}{dt}C_{m,n}(t) = \sum_j \left(-iH_{nj} - \delta_{jn}\frac{\gamma_j}{2}\right)c_m^\dagger c_j - \sum_i
$$
$$
\times \left(-iH_{im} + \delta_{im}\frac{\gamma_i}{2}\right)c_i^\dagger c_n + \gamma_i f_i \delta_{im}\delta_{mn}. \tag{E11}
$$

By considering $T = iH + \frac{1}{2}R$ with $R = \mathrm{diag}(\gamma_1, \gamma_2, \ldots, \gamma_L)$ and $P = \mathrm{diag}(\gamma_1 f_1, \gamma_2 f_2, \ldots, \gamma_L f_L)$, we obtain the more compact form,

$$
\frac{d}{dt}C(t) = -(TC + CT^\dagger) + P. \tag{E12}
$$

For a boundary-driven system, the baths are connected to the system at the ends only; hence $R_{11} = \gamma_1$, $R_{LL} = \gamma_L$ and $P_{11} = \gamma_1 f_1$, $P_{LL} = \gamma_L f_L$, and all other matrix elements of R and P are zeros. The above matrix Eq. (E12) has been solved numerically to study the correlation dynamics and transport phenomena in the open system scenario.

[1] J. Sirker, R. G. Pereira, and I. Affleck, Diffusion and ballistic transport in one-dimensional quantum systems, Phys. Rev. Lett. **103**, 216602 (2009).

[2] M. Serbyn, Z. Papić, and D. A. Abanin, Local conservation laws and the structure of the many-body localized states, Phys. Rev. Lett. **111**, 127201 (2013).

[3] D. A. Huse, R. Nandkishore, and V. Oganesyan, Phenomenology of fully many-body-localized systems, Phys. Rev. B **90**, 174202 (2014).

[4] T. Langen, T. Gasenzer, and J. Schmiedmayer, Prethermalization and universal dynamics in near-integrable quantum systems, J. Stat. Mech.: Theory Exp. (2016) 064009.

[5] R. Vasseur and J. E. Moore, Nonequilibrium quantum dynamics and transport: From integrability to many-body localization, J. Stat. Mech.: Theory Exp. (2016) 064010.

[6] X. Turkeshi and M. Schiró, Diffusion and thermalization in a boundary-driven dephasing model, Phys. Rev. B **104**, 144301 (2021).

[7] T. Prosen, Open *XXZ* spin chain: Nonequilibrium steady state and a strict bound on ballistic transport, Phys. Rev. Lett. **106**, 217206 (2011).

[8] J. Sirker, R. G. Pereira, and I. Affleck, Conservation laws, integrability, and transport in one-dimensional quantum systems, Phys. Rev. B **83**, 035115 (2011).

[9] S. S. Kondov, W. R. McGehee, W. Xu, and B. DeMarco, Disorder-induced localization in a strongly correlated atomic Hubbard gas, Phys. Rev. Lett. **114**, 083002 (2015).

[10] R. Ketzmerick, K. Kruse, S. Kraut, and T. Geisel, What determines the spreading of a wave packet? Phys. Rev. Lett. **79**, 1959 (1997).

[11] V. K. Varma, C. de Mulatier, and M. Žnidarič, Fractality in nonequilibrium steady states of quasiperiodic systems, Phys. Rev. E **96**, 032130 (2017).

[12] A. Purkayastha, S. Sanyal, A. Dhar, and M. Kulkarni, Anomalous transport in the Aubry-André-Harper model in isolated and open systems, Phys. Rev. B **97**, 174206 (2018).

[13] H. Hiramoto and S. Abe, Dynamics of an electron in quasiperiodic systems. I. Fibonacci model, J. Phys. Soc. Jpn. **57**, 230 (1988).

[14] R. P. A. Lima, F. A. B. F. de Moura, M. L. Lyra, and H. N. Nazareno, Critical wave-packet dynamics in the power-law bond disordered Anderson model, Phys. Rev. B **71**, 235112 (2005).

[15] Y. Wang, L. Zhang, S. Niu, D. Yu, and X.-J. Liu, Realization and detection of nonergodic critical phases in an optical Raman lattice, Phys. Rev. Lett. **125**, 073204 (2020).

[16] T. Cookmeyer, J. Motruk, and J. E. Moore, Critical properties of the ground-state localization-delocalization transition in the many-particle Aubry-André model, Phys. Rev. B **101**, 174203 (2020).

[17] A. M. Lacerda, J. Goold, and G. T. Landi, Dephasing enhanced transport in boundary-driven quasiperiodic chains, Phys. Rev. B **104**, 174203 (2021).

[18] Y. Takada, K. Ino, and M. Yamanaka, Statistics of spectra for critical quantum chaos in one-dimensional quasiperiodic systems, Phys. Rev. E **70**, 066203 (2004).

[19] K. Ino and M. Kohmoto, Critical properties of Harper's equation on a triangular lattice, Phys. Rev. B **73**, 205111 (2006).

[20] L. Gong and P. Tong, Fidelity, fidelity susceptibility, and von Neumann entropy to characterize the phase diagram of an extended Harper model, Phys. Rev. B **78**, 115114 (2008).

[21] G. Gumbs and P. Fekete, Hofstadter butterfly for the hexagonal lattice, Phys. Rev. B **56**, 3787 (1997).

[22] G. Jose, R. Malla, V. Srinivasan, A. Sharma, and S. Gangadharaiah, Phase diagram for the Harper model of the honeycomb lattice, J. Phys.: Condens. Matter **30**, 385603 (2018).

[23] Y. Hasegawa, Y. Hatsugai, M. Kohmoto, and G. Montambaux, Stabilization of flux states on two-dimensional lattices, Phys. Rev. B **41**, 9174 (1990).

[24] M. Kohmoto, Entropy function for multifractals, Phys. Rev. A **37**, 1345 (1988).

[25] K. Ikezawa and M. Kohmoto, Energy spectrum and the critical wavefunctions of the quasiperiodic Harper

equation—the silver mean case, J. Phys. Soc. Jpn. **63**, 2261 (1994).

[26] S. Ghosh, M. Singh, and S. Gangadharaiah, Magnetization dynamics in the XX spin chain model via multiparticle state, Phys. Rev. B **104**, 144306 (2021).

[27] T. Jin, T. Gautié, A. Krajenbrink, P. Ruggiero, and T. Yoshimura, Interplay between transport and quantum coherences in free fermionic systems, J. Phys. A: Math. Theor. **54**, 404001 (2021).

[28] D. Pereira and E. J. Mueller, Dynamics of spin helices in the one-dimensional *XX* model, Phys. Rev. A **106**, 043306 (2022).

[29] T. Antal, Z. Rácz, A. Rákos, and G. M. Schütz, Transport in the XX chain at zero temperature: Emergence of flat magnetization profiles, Phys. Rev. E **59**, 4912 (1999).

[30] V. Hunyadi, Z. Rácz, and L. Sasvári, Dynamic scaling of fronts in the quantum *XX* chain, Phys. Rev. E **69**, 066103 (2004).

[31] S. Singha Roy, G. Ramírez, S. N. Santalla, G. Sierra, and J. Rodríguez-Laguna, Exotic correlation spread in free-fermionic states with initial patterns, Phys. Rev. B **105**, 214306 (2022).

[32] Y. Wang and B. M. Terhal, Preparing Dicke states in a spin ensemble using phase estimation, Phys. Rev. A **104**, 032407 (2021).

[33] G.-P. Guo, C.-F. Li, J. Li, and G.-C. Guo, Scheme for the preparation of multiparticle entanglement in cavity QED, Phys. Rev. A **65**, 042102 (2002).

[34] G. Barontini, R. Labouvie, F. Stubenrauch, A. Vogler, V. Guarrera, and H. Ott, Controlling the dynamics of an open many-body quantum system with localized dissipation, Phys. Rev. Lett. **110**, 035302 (2013).

[35] P. N. Jepsen, J. Amato-Grill, I. Dimitrova, W. W. Ho, E. Demler, and W. Ketterle, Spin transport in a tunable Heisenberg model realized with ultracold atoms, Nature (London) **588**, 403 (2020).

[36] A. N. Ciavarella, S. Caspar, M. Illa, and M. J. Savage, State preparation in the Heisenberg model through adiabatic spiraling, Quantum **7**, 970 (2023).

[37] P. G. Harper, Single band motion of conduction electrons in a uniform magnetic field, Proc. Phys. Soc. A **68**, 874 (1955).

[38] D. R. Hofstadter, Energy levels and wave functions of Bloch electrons in rational and irrational magnetic fields, Phys. Rev. B **14**, 2239 (1976).

[39] F. Piéchon, Anomalous diffusion properties of wave packets on quasiperiodic chains, Phys. Rev. Lett. **76**, 4372 (1996).

[40] J. Zhong, R. B. Diener, D. A. Steck, W. H. Oskay, M. G. Raizen, E. W. Plummer, Z. Zhang, and Q. Niu, Shape of the quantum diffusion front, Phys. Rev. Lett. **86**, 2485 (2001).

[41] G. S. Ng and T. Kottos, Wavepacket dynamics of the nonlinear Harper model, Phys. Rev. B **75**, 205120 (2007).

[42] B. Bertini, F. Heidrich-Meisner, C. Karrasch, T. Prosen, R. Steinigeweg, and M. Žnidarič, Finite-temperature transport in one-dimensional quantum lattice models, Rev. Mod. Phys. **93**, 025003 (2021).

[43] T. Prosen and B. Žunkovič, Exact solution of Markovian master equations for quadratic Fermi systems: Thermal baths, open XY spin chains and non-equilibrium phase transition, New J. Phys. **12**, 025016 (2010).

[44] M. Lewenstein, A. Sanpera, V. Ahufinger, B. Damski, A. Sen(De), and U. Sen, Ultracold atomic gases in optical lattices: Mimicking condensed matter physics and beyond, Adv. Phys. **56**, 243 (2007).

[45] I. Bloch, J. Dalibard, and W. Zwerger, Many-body physics with ultracold gases, Rev. Mod. Phys. **80**, 885 (2008).

[46] J. Struck, C. Ölschläger, M. Weinberg, P. Hauke, J. Simonet, A. Eckardt, M. Lewenstein, K. Sengstock, and P. Windpassinger, Tunable gauge potential for neutral and spinless particles in driven optical lattices, Phys. Rev. Lett. **108**, 225304 (2012).

[47] H. Miyake, G. A. Siviloglou, C. J. Kennedy, W. C. Burton, and W. Ketterle, Realizing the Harper Hamiltonian with laser-assisted tunneling in optical lattices, Phys. Rev. Lett. **111**, 185302 (2013).

[48] S. Safaei, C. Miniatura, and B. Grémaud, Triangular and honeycomb lattices of cold atoms in optical cavities, Phys. Rev. A **92**, 043810 (2015).